SHORT-TIMESCALE MONITORING OF THE X-RAY, UV, AND BROAD DOUBLE-PEAK EMISSION LINE OF THE NUCLEUS OF NGC 1097

Jaderson S. Schimoia[1,2], Thaisa Storchi-Bergmann[1,3], Dirk Grupe[4,10], Michael Eracleous[5,11,12],
Bradley M. Peterson[2,6], Jack A. Baldwin[7], Rodrigo S. Nemmen[8,13,14,15], and Cláudia Winge[9]

[1] Instituto de Física, Universidade Federal do Rio Grande do Sul, Campus do Vale, Porto Alegre, RS, Brazil; silva.schimoia@ufrgs.br
[2] Department of Astronomy, The Ohio State University, 140 West 18th Avenue, Columbus, OH 43210, USA
[3] Harvard-Smithsonian Center for Astrophysics, 60 Garden Street, Cambridge, MA 02138, USA
[4] Space Science Center, Morehead State University, 235 Martindale Drive, Morehead, KY 40351, USA
[5] Department of Astronomy and Astrophysics and Institute for Gravitation and the Cosmos, Pennsylvania State University,
525 Davey Lab, University Park, PA 16802, USA
[6] Center for Cosmology and AstroParticle Physics, The Ohio State University,
191 West Woodruff Avenue, Columbus, OH 43210, USA
[7] Department of Physics and Astronomy, Michigan State University, East Lansing, MI 48864, USA
[8] Instituto de Astronomia, Geofísica e Ciências Atmosféricas, Universidade de São Paulo, São Paulo, SP 05508-090, Brazil
[9] Gemini South Observatory, c/o AURA Inc., Casilla 603, La Serena, Chile
Received 2014 July 28; accepted 2014 November 5; published 2015 February 10

ABSTRACT

Recent studies have suggested that the short-timescale ($\lesssim$7 days) variability of the broad ($\sim$10,000 km s^{-1}) double-peaked Hα profile of the LINER nucleus of NGC 1097 could be driven by a variable X-ray emission from a central radiatively inefficient accretion flow. To test this scenario, we have monitored the NGC 1097 nucleus in X-ray and UV continuum with *Swift* and the Hα flux and profile in the optical spectrum using SOAR and Gemini-South from 2012 August to 2013 February. During the monitoring campaign, the Hα flux remained at a very low level—three times lower than the maximum flux observed in previous campaigns and showing only limited ($\sim$20%) variability. The X-ray variations were small, only $\sim$13% throughout the campaign, while the UV did not show significant variations. We concluded that the timescale of the Hα profile variation is close to the sampling interval of the optical observations, which results in only a marginal correlation between the X-ray and Hα fluxes. We have caught the active galaxy nucleus in NGC 1097 in a very low activity state, in which the ionizing source was very weak and capable of ionizing just the innermost part of the gas in the disk. Nonetheless, the data presented here still support the picture in which the gas that emits the broad double-peaked Balmer lines is illuminated/ionized by a source of high-energy photons which is located interior to the inner radius of the line-emitting part of the disk.

Key words: accretion, accretion disks – galaxies: individual (NGC 1097) – galaxies: nuclei – galaxies: Seyfert – line: profiles

1. INTRODUCTION

The energy emitted by active galaxy nuclei (AGNs) is provided by accretion of mass onto a supermassive black hole (SMBH), via an accretion disk, whose emission is observed in the UV continuum of Seyfert galaxies and quasars (e.g., Frank et al. 2002). The optical spectra of some AGN show extremely broad ($\sim$10,000 km s^{-1}) double-peaked emission lines that are thought to originate in the outer extension of the accretion disk. Indeed, models of ionized gas emission rotating in a relativistic Keplerian accretion disk around an SMBH have been generally successful in accounting for the double-peaked profiles (Chen et al. 1989; Chen & Halpern 1989; Storchi-Bergmann et al. 2003; Strateva et al. 2003; Lewis et al. 2010). These models explain self-consistently most observable features of the double-peaked profiles (Eracleous & Halpern 2003). Long

timescale monitoring (years to decades) has revealed variability of the double-peaked profiles in several objects, including the radio galaxy 3C390.3 (Shapovalova et al. 2010), the LINER NGC 1097 (Storchi-Bergmann et al. 2003), the radio galaxy Pictor A, and other radio-loud AGNs (Gezari et al. 2007; Lewis et al. 2010).

The variations in double-peaked profiles can provide an effective probe of disk models and lead to understanding of the physical mechanisms that cause profile variability. For this reason, we have monitored the double-peaked Hα profile in the nuclear spectrum of NGC 1097. We were fortunate enough to obtain a few Gemini-South spectra separated by less than a week, which revealed much shorter timescale profile variability than had been seen before in this source. Our observations constrain the variability timescale of the integrated flux of the profile and the velocity separation between the blue and red peaks to approximately seven days (Schimoia et al. 2012). This is the shortest timescale variability ever seen in the double-peaked profile of this object, and coincides with the estimated light travel time between the nucleus and the line-emitting region of the disk.

The short-timescale variations suggest that the line emission is driven by the central source. A number of studies have compared the available energy due to local viscous dissipation in the accretion disk with the observed luminosity of emission lines and concluded that there is indeed the need for an external

---

ionizing source to power the observed luminosity of the double-peaked emission lines. This has been argued by Eracleous & Halpern (1994), Strateva et al. (2006, 2008), and Luo et al. (2013). In the case of NGC 1097, Nemmen et al. (2006) have proposed that the ionizing source is a radiatively inefficient accretion flow (RIAF; Narayan & McClintock 2008) located in the center (or inner rim) of the disk. The seven-day timescale is consistent with an origin of the emission-line variability as a reverberation signal of the varying X-ray emission from the inner RIAF in the line-emitting portion of the disk.

In our previous studies of profile variability in the spectrum of NGC 1097 (Schimoia et al. 2012) we also found an inverse correlation between the flux of the line and the velocity separation between the two peaks of the profile, confirming the previous result reported by Storchi-Bergmann et al. (2003). This inverse correlation also supports the reverberation scenario: when the flux is higher, the RIAF at the center is more luminous and illuminates/ionizes farther out in the accretion disk, where the disk rotational velocities are lower (thus the profile is narrower); conversely, when the flux from the RIAF is lower, the disk emissivity is weighted more heavily toward smaller radii where the velocities are higher, hence the profile is broader. A similar behavior is also observed in 3C 390.3 by Shapovalova et al. (2001, see their Figure 4).

In order to test the hypothesis that the Hα variability is a reverberation response to variations of the X-ray and UV continuum emitted by the inner RIAF, we undertook a campaign to monitor the X-ray and Hα emission in NGC 1097. From 2012 August to 2013 February, we monitored the emission from the nucleus of NGC 1097 in three different wavelengths bands. The high-energy continuum (presumably emitted by the RIAF) was monitored with the *Swift* satellite, using the X-ray telescope (XRT) telescope to obtain X-ray fluxes and the UVOT(M2) to obtain the UV fluxes. The spectral monitoring of the Hα double-peaked profile was performed using the GOODMAN spectrograph at the SOAR telescope. In this contribution, we report on the results of this campaign. In Section 2, we describe the observations and the data reduction and, in Section 3, we present the measurements of the properties of the Hα double-peaked profile and the flux measurements of X-ray/UV bands as well as the main results from our monitoring campaign. In Section 4, we discuss the results and their physical implications to the reverberation scenario and the emitting structure of the double-peaked profile. Our conclusions are summarized in Section 5.

2. OBSERVATIONS AND DATA REDUCTION

2.1. X-Ray and Ultraviolet Observations with Swift

Observations were made with X-ray and ultraviolet (UV) telescopes on *Swift* between 2012 July 26 and 2013 January 30 (MJD[16] 56134 to 56327).

The *Swift* XRT (Burrows et al. 2005) was operated in photon counting mode (Hill et al. 2004). The data were reduced by the task `xrtpipeline` version 0.12.6., which is included in the HEASOFT package 6.12. Source counts were measured inside a circle of radius $47''$ and the background was determined from a source-free region of radius of $235''$ using the task `xselect` (version 2.4b). Auxiliary response files were created using the XRT task `xrtmkarf`. The spectra were rebinned with

20 counts per bin using the task `grppha` and the response files `swxpc0to12s6_20010101v013.rmf` were applied. The rebinned spectra were modeled over the range 0.3–10 keV in XSPEC v.12.7 with a single power law and correction for Galactic absorption corresponding to a hydrogen column density $N_H = 2.03 \times 10^{20}$ cm^{-2} (Kalberla et al. 2005), which is very close to the value of $N_H = 2.3 \times 10^{20}$ cm^{-2} determined from a *Chandra* observation by Nemmen et al. (2006).

We analyzed all available data obtained with the *Swift* UV/Optical Telescope (UVOT; Roming et al. 2005) during this period. We restrict our attention to data obtained through the UVM2 (2246 Å) filter as it is the cleanest of the UVOT filters (Breeveld et al. 2010). We employed the UVOT software task `uvotsource` to extract counts within a circular region of $3''.0$ radius for the nucleus of NGC 1097 and used $20''$ radius to determine the background. The UVOT count rates were aperture corrected and then converted into magnitudes and fluxes based on the most recent UVOT calibration as described by Poole et al. (2008) and Breeveld et al. (2010). The flux measurements were corrected for Galactic reddening ($E_{B-V} = 0.027$ mag) following the corrections given by Roming et al. (2009), based on standard reddening correction curves from Cardelli et al. (1989). X-ray and UV measurements from *Swift* are given in Table 1.

2.2. Optical Observations with SOAR

The Hα region of the optical spectrum was monitored at the SOAR Telescope using the Goodman High-Throughput Spectrograph in long-slit mode. Observations were obtained approximately every 7 days in queue mode from MJD56147 to MJD56319 for a total of 22 epochs (Program SO2012B-020). A few scheduled observations were lost to poor weather so the actual mean interval between observations is ∼7.5 days. A log of observations appears in Table 2.

The observations employed a 600 l mm^{-1} grating, yielding a dispersion of 0.065 nm pixel^{-1} in the "Mid" mode. A GG455 filter was used to block second-order contamination. This setup provides wavelength coverage 450–725 nm and spectral resolution of ∼0.55 nm, measured as the FWHM of the lines in the arc spectrum. The spectrograph slit was set to a projected width of $1''.03$ (∼80 pc at the galaxy), because it is usually larger than the average seeing during the observations. The same slit width was used in our previous observations (SB03), which allows us to scale the new spectra to match the narrow emission line fluxes observed in our previous studies. This allows us to "normalize" the spectra to a common flux scale.

2.3. Gemini Data

Motivated by the low Hα flux in the SOAR spectra obtained early in this campaign compared to what had been observed previously (Schimoia et al. 2012), a single long-slit spectrum was obtained with the Gemini-South Multi-Object Spectrograph on MJD56173. This observation was obtained as part of an active "Poor Weather" project on the Gemini-South telescope (Program GS-2012A-Q-86). For this observation, we used a slit width of $1''.0$, the B600 grating, and a GG455 filter. The resulting spectrum covers the range from 510 nm to 800 nm with a resolution of ∼0.45 nm. The data were reduced using the standard procedures in the *IRAF*[17] software package.

Table 1
X-ray and UV Measurements from *Swift*

UT Date	MJD	F_X	α_X	F(M2)
2012 Jul 26	56134.374	$3.88^{+1.15}_{-0.55}$	0.58 ± 0.32	0.92 ± 0.06
2012 Jul 30	56138.928	$3.47^{+0.60}_{-0.43}$	0.59 ± 0.30	1.05 ± 0.07
2012 Aug 3	56142.342	$4.93^{+0.62}_{-0.58}$	0.83 ± 0.40	1.01 ± 0.07
2012 Aug 7	56146.819	$5.94^{+0.82}_{-0.55}$	0.97 ± 0.39	1.01 ± 0.07
2012 Aug 11	56150.781	$2.70^{+0.50}_{-0.30}$	1.15 ± 0.46	1.01 ± 0.07
2012 Aug 15	56154.631	$5.17^{+0.66}_{-0.74}$	0.65 ± 0.36	1.00 ± 0.06
2012 Aug 19	56158.967	$3.63^{+0.60}_{-0.31}$	0.72 ± 0.33	0.92 ± 0.06
2012 Aug 23	56162.712	$4.20^{+0.77}_{-0.55}$	0.76 ± 0.29	0.88 ± 0.06
2012 Aug 27	56166.786	$3.65^{+0.51}_{-0.29}$	0.91 ± 0.30	1.02 ± 0.07
2012 Aug 31	56170.586	$4.00^{+0.61}_{-0.63}$	0.75 ± 0.29	0.99 ± 0.06
2012 Sep 4	56174.538	$2.69^{+0.28}_{-0.23}$	1.17 ± 0.32	0.98 ± 0.06
2012 Sep 8	56178.213	$2.95^{+0.40}_{-0.32}$	1.03 ± 0.33	0.98 ± 0.06
2012 Sep 12	56182.295	$3.45^{+0.52}_{-0.43}$	0.80 ± 0.34	0.96 ± 0.06
2012 Sep 16	56186.561	$3.80^{+0.76}_{-0.50}$	0.99 ± 0.35	0.98 ± 0.06
2012 Sep 20	56190.781	$4.28^{+1.89}_{-0.56}$	1.12 ± 0.90	1.07 ± 0.09
2012 Sep 24	56194.715	$8.41^{+4.98}_{-2.28}$	0.28 ± 0.67	0.98 ± 0.09
2012 Oct 2	56202.063	$4.23^{+0.61}_{-0.49}$	0.71 ± 0.28	0.91 ± 0.06
2012 Oct 6	56206.406	$3.32^{+0.71}_{-0.39}$	0.73 ± 0.33	0.96 ± 0.06
2012 Oct 10	56210.958	$3.61^{+1.10}_{-0.46}$	0.76 ± 0.40	0.93 ± 0.06
2012 Oct 14	56214.900	$3.24^{+0.34}_{-0.42}$	0.81 ± 0.30	0.94 ± 0.06
2012 Oct 18	56218.039	$3.14^{+0.46}_{-0.52}$	0.69 ± 0.32	0.99 ± 0.06
2012 Oct 22	56222.231	$4.35^{+0.46}_{-0.52}$	0.84 ± 0.27	0.95 ± 0.06
2012 Oct 26	56226.722	$2.89^{+0.50}_{-0.40}$	0.91 ± 0.36	0.96 ± 0.06
2012 Oct 30	56230.864	$2.52^{+0.46}_{-0.29}$	1.26 ± 0.48	0.89 ± 0.06
2012 Nov 3	56234.130	$2.09^{+0.48}_{-0.26}$	1.37 ± 0.46	0.96 ± 0.06
2012 Nov 7	56238.066	$3.39^{+0.57}_{-0.56}$	0.61 ± 0.35	0.97 ± 0.06
2012 Nov 15	56246.648	$2.95^{+0.56}_{-0.44}$	0.87 ± 0.38	0.97 ± 0.06
2012 Nov 19	56250.828	$3.15^{+0.39}_{-0.42}$	0.79 ± 0.33	0.95 ± 0.06
2012 Nov 27	56258.854	$3.12^{+0.72}_{-0.52}$	0.78 ± 0.36	0.94 ± 0.06
2012 Dec 1	56262.323	$2.87^{+0.47}_{-0.40}$	0.96 ± 0.37	0.85 ± 0.05
2012 Dec 5	56266.800	$2.01^{+0.43}_{-0.25}$	0.90 ± 0.36	0.87 ± 0.05
2012 Dec 9	56270.465	$3.05^{+0.51}_{-0.38}$	1.08 ± 0.31	0.95 ± 0.06
2012 Dec 13	56274.674	$4.35^{+0.82}_{-0.60}$	0.77 ± 0.39	0.91 ± 0.06
2012 Dec 17	56278.610	$3.00^{+0.68}_{-0.40}$	0.95 ± 0.40	0.88 ± 0.06
2012 Dec 21	56282.482	$3.35^{+0.59}_{-0.40}$	1.04 ± 0.37	0.88 ± 0.05
2012 Dec 25	56286.829	$5.05^{+1.08}_{-0.75}$	0.67 ± 0.35	0.93 ± 0.06
2012 Dec 29	56290.834	$3.36^{+0.64}_{-0.66}$	0.76 ± 0.32	0.89 ± 0.06
2013 Jan 2	56294.041	$2.78^{+0.62}_{-0.27}$	0.52 ± 0.60	0.88 ± 0.06
2013 Jan 6	56298.645	$2.99^{+0.59}_{-0.49}$	0.62 ± 0.32	0.89 ± 0.06
2013 Jan 10	56302.618	$2.04^{+0.46}_{-0.24}$	1.01 ± 0.43	0.87 ± 0.06
2013 Jan 14	56306.397	$2.49^{+0.60}_{-0.38}$	0.69 ± 0.43	0.90 ± 0.06
2013 Jan 18	56310.286	$2.90^{+0.46}_{-0.40}$	1.06 ± 0.30	0.97 ± 0.06
2013 Jan 22	56314.755	$3.66^{+0.52}_{-0.35}$	1.00 ± 0.28	0.95 ± 0.06
2013 Jan 26	56318.159	$2.62^{+0.37}_{-0.27}$	1.05 ± 0.33	0.93 ± 0.06
2013 Jan 30	56322.089	$3.82^{+0.55}_{-0.32}$	0.74 ± 0.29	0.85 ± 0.05

Notes. Column 1 gives the date of observations while Column 2 gives the Modified Julian Date (JD−2400000.5). Column 3 gives the 0.3–10 keV flux in units of 10^{-12} erg s^{-1} cm^{-2} and the X-ray power-law slope appears in Column 4. Column 5 gives the UV M2 (~2246 Å) flux in units of 10^{-15} erg s^{-1} cm^{-2}.

The resulting GMOS spectrum demonstrated that despite the low Hα flux, the double-peaked profiles obtained at SOAR were sufficiently reliable for detailed analysis.

Table 2
Observation Log

Telescope	UT Date	MJD	Exposure Time (s)	P.A. (°)
SOAR	2012 Aug 7	56147.356	3×1200	260
SOAR	2012 Aug 9	56149.368	3×1200	262
SOAR	2012 Aug 10	56150.360	3×1200	262
SOAR	2012 Aug 24	56164.349	2×1200	264
SOAR	2012 Aug 31	56171.388	2×1200	90
Gemini South	2012 Sep 03	56173.305	6×600	280
SOAR	2012 Sep 8	56179.370	3×1200	89
SOAR	2012 Sep 16	56187.222	3×1200	260
SOAR	2012 Sep 23	56194.256	2×1500	90
SOAR	2012 Sep 27	56198.175	5×1200	257
SOAR	2012 Oct 12	56213.316	3×1200	94
SOAR	2012 Oct 18	56219.316	3×1200	96
SOAR	2012 Oct 25	56226.048	3×1200	251
SOAR	2012 Oct 28	56229.229	3×1200	90
SOAR	2012 Nov 2	56234.086	3×1200	360
SOAR	2012 Nov 12	56244.074	3×1200	259
SOAR	2012 Nov 23	56255.068	3×1800	261
SOAR	2012 Dec 8	56270.206	3×1800	98
SOAR	2012 Dec 15	56277.142	3×1800	95
SOAR	2012 Dec 23	56285.097	3×1200	360
SOAR	2012 Dec 28	56290.074	3×1200	91
SOAR	2013 Jan 17	56310.047	4×1200	93
SOAR	2013 Jan 26	56319.067	3×1200	97

Notes. The telescope used is given in Column 1 and the date of observation appears in Column 2 while Column 3 gives the Modified Julian Date (JD−2400000.5). Columns 4 and 5 give the exposure time and slit position angle, respectively.

3. DATA ANALYSIS

3.1. The Hα Profile

3.1.1. Nuclear Extractions and the Stellar Population Contribution

We extracted the nuclear spectra using windows of $1\farcs03 \times 1\farcs0$ and $1\farcs0 \times 1\farcs0$ for SOAR and Gemini data, respectively (Figure 1). The nuclear extraction windows were centered at the peak of the continuum emission, which coincides with the location of the unresolved source of the broad Hα line. Since the nuclear spectrum shows strong absorption lines from the underlying stellar population (Figure 1), we subtracted the stellar population contribution in order to isolate the Hα profile. For each epoch, we extracted and then averaged two additional spectra with extraction windows centered $2\farcs0$ away from the nuclear window (Figure 1). The average extranuclear spectra display the same absorption features as the nuclear spectra, and are only weakly "contaminated" by narrow emission lines which were excised by using a synthetic spectrum obtained by running the `starlight-v04` code of Cid Fernandes et al. (2005) as a template. We assume that this spectrum is representative of the nuclear stellar population and scale and subtract it from the nuclear spectrum, thus isolating the emission-line spectrum, as shown in Figure 1. As in our previous studies, the nuclear spectrum shows no detectable non-stellar continuum emission, only line emission.

We then normalized in flux the nuclear emission spectra using as reference a previous flux-calibrated spectrum from 1991 November 2 (Storchi-Bergmann et al. 1993), as we have in previous studies (Storchi-Bergmann et al. 2003; Schimoia et al. 2012). We assume that the fluxes in [N II] λλ6548, 6584, [S II] λλ6717, 6731, and the narrow component of Hα
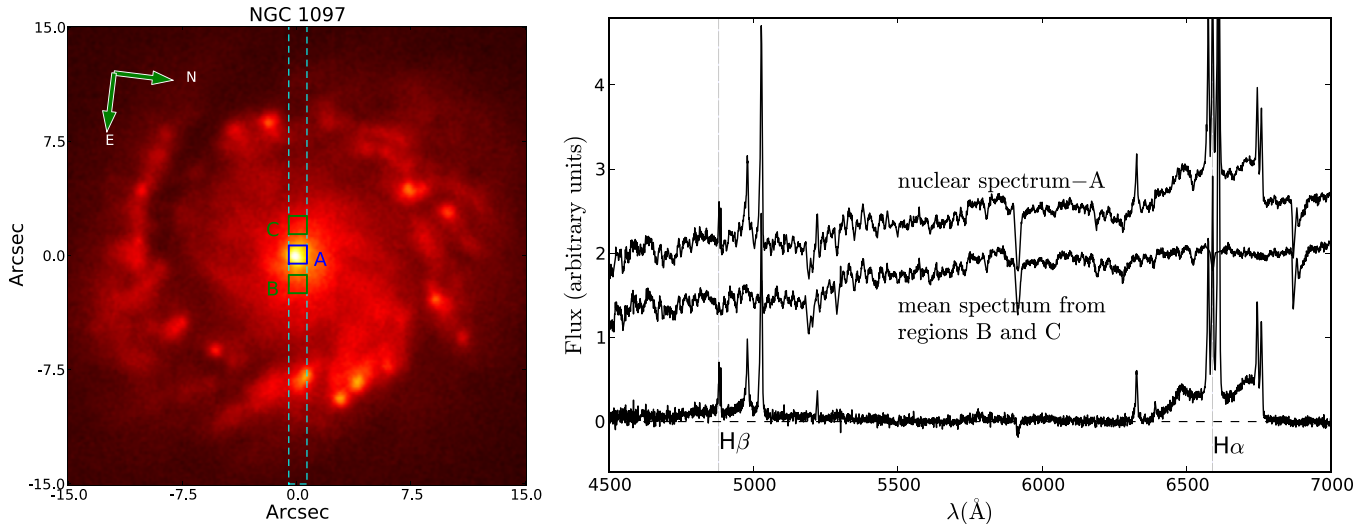
Figure 1. Left: acquisition image of the nuclear region of NGC 1097 from the SOAR observation of MJD56194. The cyan dashed line represents the slit (width of 1″03). The blue square (A) shows the extraction window (1″03 × 1″0) of the nuclear spectrum. The green squares (B and C), centered at 2″0 from the nucleus show the windows used to extract stellar population spectra. Right: (a) top: nuclear spectrum extracted from window A; (b) middle: mean spectrum of B and C, adopted as representative of the nuclear stellar population; (c) bottom: difference between (a) and (b) (after scaling), which isolates the nuclear emission.

have not varied since our 1991 observation because of the long light travel time across the region as well as the long recombination time at low densities (although these assumptions may not hold for higher-ionization narrow lines, see Peterson et al. 2013). Hereafter we refer to the flux-calibrated starlight-corrected nuclear emission spectra simply as the "nuclear emission spectra."

As we noted earlier, the broad Hα flux is lower than it had been in our earlier observations, and consequently some of the spectra are noisy. This leads to some ambiguity in measuring profile parameters (as described in the next section) such as the wavelengths of the red and blue peaks. We therefore smoothed the spectra with a Gaussian function. We experimented with Gaussian smoothing functions between one and five times the spectral resolution (i.e., FWHM between 5.5 and 27.5 Å), finally settling on FWHM = 11 Å. This resulted in much better defined profile parameters for noisier spectra without altering the measurements for the less noisy spectra.

3.1.2. Salient Features of the Hα Profile Variations

The smoothed nuclear emission spectra are shown in Figure 2. The most conspicuous characteristics of the evolution of the profile during the monitoring campaign are:

1. The double-peaked profile remained asymmetric, although the relative intensity of the blue and red peaks changed during the campaign. At the beginning of the observations, MJD56147, the maximum flux of the blue peak, F_B, was slightly stronger than the maximum flux of the red peak, F_R. The profile changed gradually until the red peak was much stronger than the blue peak by MJD56194. After that, the blue peak became increasingly prominent, becoming stronger than the red peak by MJD56277. This is similar to the results of our previous studies that showed that the relative intensity of the blue and red peaks changes on a timescale of months (Storchi-Bergmann et al. 2003; Schimoia et al. 2012).

2. Besides the changes in the relative intensity of the peaks, the integrated flux of the broad Hα line, F_{broad}, also varied

significantly. The first remarkable rise in F_{broad} occurred in the interval MJD56187–56194, when it changed from 62.5 ($\pm$6.9) $\times$ 10^{-15} erg s^{-1} cm^{-2} to 107.9 ($\pm$4.4) $\times$ 10^{-15} erg s^{-1} cm^{-2}, an increase of $\sim$70% in just six days. A second, even larger, flux increase of $\sim$90% occurred in the interval MJD56285–56290, when the Hα flux increased from 43.8 ($\pm$8.2) $\times$ 10^{-15} erg s^{-1} cm^{-2} to 83.4 ($\pm$5.3) $\times$ 10^{-15} erg s^{-1} cm^{-2} in only five days.

3. After MJD56277, the red peak became less well-defined, with a shape more like a "plateau." Similar behavior is seen on the blue side of the profile in the observation of MJD56310. By the final observation of the campaign on MJD56319, the double-peaked nature of the profile is barely discernible.

3.1.3. Model-independent Parameterization of the Double-peaked Profile

Prior to making measurements to parameterize the broad Hα profile, we must first remove the very strong narrow emission lines that are still present in the spectrum. We attempted to remove these features by simultaneously fitting three Gaussians to the Hα narrow component and the [N II] λλ6548, 6584 lines and two more Gaussians to the [S II] λλ6717, 6731 doublet. After removing the narrow components, we made the following measurements: λ_i is the initial wavelength, defined as the wavelength at which the flux of the blue side reaches zero intensity within the uncertainties. Similarly, λ_f is the final wavelength where the flux of the red side of the profile reaches zero intensity. Together these two parameters define the wavelength range of the double-peaked profile. F_B is the maximum intensity of the blue peak (or blue side) of the profile and λ_B is the wavelength where this maximum occurs, while F_R is the maximum intensity of the red peak (or red side) of the profile and λ_R the wavelength where it occurs. We obtained the integrated flux in the broad component of Hα F_{broad} by integrating the flux underneath the profile from λ_i to λ_f. Figure 3 illustrates all these properties, including the results of fitting and subtracting the contribution of the narrow lines. The resulting measurements are listed in Table 3. For most spectra,
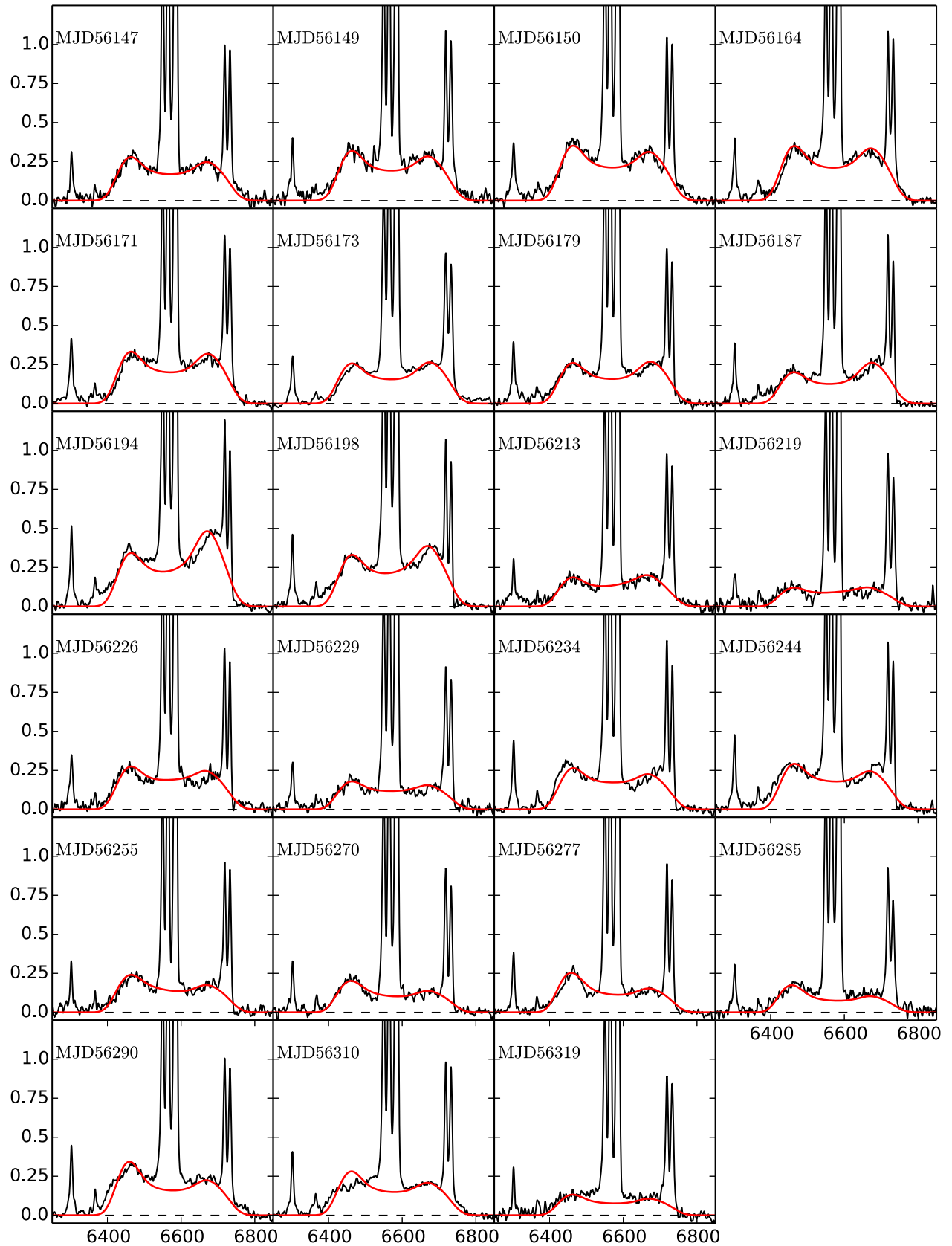
Figure 2. Resulting spectra of each epoch after the subtraction of the stellar population contribution and calibration through the fluxes of the narrow emission lines (which do not vary on such short timescales). For each frame the vertical axis is flux in units of 10^{-15} erg s^{-1} cm^{-2} Å^{-1} while the horizontal axis is wavelength in units of Å. The red solid line is the best fit of the accretion disk model to the data (see Section 4.1 for details).

Table 3
Measurements of the Characteristics of the Double-peaked Profile

UT Date	MJD	F_{broad}	λ_i	λ_f	λ_B	λ_R	F_B	F_R
2012 Aug 7	56147.356	71.9 ± 8.9	6381	6784	6469.6 ± 1.1	6665.3 ± 1.8	0.264 ± 0.088	0.231 ± 0.087
2012 Aug 9	56149.368	87.6 ± 10.5	6371	6793	6467.0 ± 4.1	6666.6 ± 5.3	0.304 ± 0.100	0.279 ± 0.099
2012 Aug 10	56150.360	93.3 ± 8.0	6361	6793	6469.9 ± 2.7	6661.2 ± 4.3	0.350 ± 0.074	0.295 ± 0.073
2012 Aug 24	56164.349	90.3 ± 5.7	6367	6781	6473.5 ± 3.4	6660.0 ± 5.5	0.309 ± 0.054	0.295 ± 0.054
2012 Aug 31	56171.388	85.4 ± 5.4	6364	6789	6476.8 ± 2.3	6672.4 ± 1.3	0.291 ± 0.050	0.275 ± 0.050
2012 Sep 3	56173.305	70.9 ± 7.8	6365	6772	6466.8 ± 1.2	6685.3 ± 7.7	0.220 ± 0.078	0.236 ± 0.074
2012 Sep 8	56179.370	70.4 ± 7.1	6365	6772	6463.9 ± 1.2	6684.3 ± 3.1	0.238 ± 0.070	0.247 ± 0.070
2012 Sep 16	56187.222	62.5 ± 6.9	6370	6755	6464.8 ± 2.2	6683.2 ± 1.9	0.197 ± 0.070	0.248 ± 0.071
2012 Sep 23	56194.256	107.9 ± 4.4	6356	6775	6467.4 ± 2.1	6679.3 ± 2.0	0.337 ± 0.042	0.438 ± 0.042
2012 Sep 27	56198.175	92.4 ± 7.1	6365	6776	6465.1 ± 4.6	6669.3 ± 3.7	0.301 ± 0.068	0.354 ± 0.068
2012 Oct 12	56213.316	51.2 ± 9.5	6375	6783	6460.5 ± 2.1	6685.4 ± 2.5	0.169 ± 0.092	0.182 ± 0.093
2012 Oct 18	56219.316	30.6 ± 9.0	6386	6763	6457.8 ± 1.8	6683.7 ± 2.4	0.118 ± 0.045	0.101 ± 0.095
2012 Oct 25	56226.048	66.8 ± 8.3	6374	6800	6465.2 ± 2.3	6682.9 ± 2.4	0.246 ± 0.078	0.206 ± 0.078
2012 Oct 28	56229.229	42.5 ± 8.4	6375	6786	6453.4 ± 2.5	6687.3 ± 4.6	0.171 ± 0.081	0.134 ± 0.081
2012 Nov 2	56234.086	66.5 ± 4.5	6372	6780	6458.3 ± 3.6	6685.2 ± 2.7	0.269 ± 0.044	0.222 ± 0.044
2012 Nov 12	56244.074	75.5 ± 6.4	6363	6785	6475.2 ± 1.6	6678.2 ± 3.9	0.270 ± 0.060	0.256 ± 0.061
2012 Nov 23	56255.068	53.6 ± 8.1	6377	6751	6463.9 ± 3.5	6677.2 ± 5.1	0.219 ± 0.086	0.169 ± 0.086
2012 Dec 8	56270.206	42.7 ± 6.7	6375	6763	6464.0 ± 0.5	6669.0 ± 2.1	0.198 ± 0.071	0.124 ± 0.071
2012 Dec 15	56277.142	47.2 ± 4.8	6369	6762	6471.1 ± 2.8	6670.2 ± 2.0	0.226 ± 0.049	0.133 ± 0.049
2012 Dec 23	56285.097	43.8 ± 8.2	6381	6787	6468.9 ± 2.9	6672.0 ± 2.8	0.179 ± 0.090	0.123 ± 0.046
2012 Dec 28	56290.074	83.4 ± 5.3	6363	6794	6467.6 ± 1.8	. . .	0.307 ± 0.135	. . .
2013 Jan 17	56310.047	67.4 ± 5.7	6367	6788	. . .	6672.2 ± 5.1	. . .	0.202 ± 0.047
2013 Jan 26	56319.067	40.5 ± 8.0	6376	6753	6496.32 ± 5.2	6686.7 ± 8.5	0.140 ± 0.047	0.125 ± 0.106

Notes. Column 1 gives the date of observations while Column 2 gives the Modified Julian Date (JD−2400000.5). In Column 3, the integrated flux of the double-peaked profile in units of 10^{-15} erg s^{-1} cm^{-2} is shown. In Column 4, the initial wavelength of the double-peaked profile is given and in Column 5 the corresponding final wavelength is given; both are given in Å. In Columns 6 and 7, respectively, the wavelengths in Å where the maximum intensity of the blue and the red peaks occur are given. In Columns 8 and 9 the values of the maximum intensity of the blue and red peaks, respectively, in units of 10^{-15} erg s^{-1} cm^{-2} Å^{-1} are given.
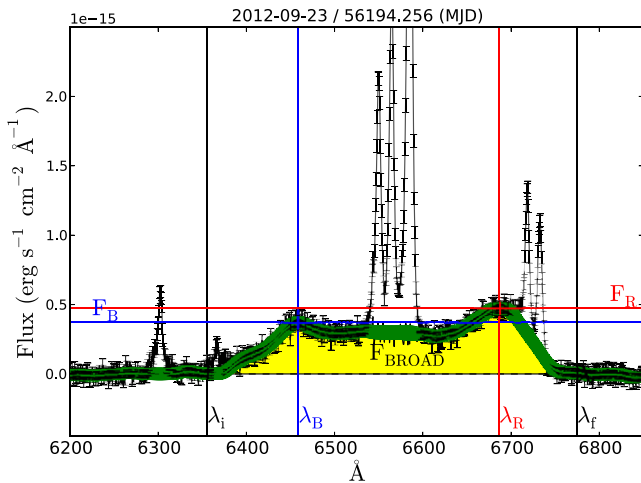
Figure 3. Visual representation of the measured properties of the Hα double-peaked profile for the observation of MJD56194. The vertical black lines mark λ_i and λ_f (respectively the lower and upper wavelength limits of the double-peaked profile). The horizontal blue line marks the maximum flux value for the blue peak, F_B, while the vertical blue line marks λ_B, the wavelength where F_B occurs. The maximum flux of the red peak F_R is marked by the horizontal red line, while λ_R is marked by the vertical red line. The green strip represents the Gaussian smoothing of the spectrum. The yellow region represents F_{broad}, after subtracting the contribution of the narrow emission lines.

it was possible to make reliable measurements of the properties describe above. However, the irregular profiles in the final observations (from MJD56285 on) preclude characterization of the blue and red peaks.

3.2. Time-series Analysis

In this section, we characterize the variability of the X-ray and UV continuum and the integrated flux F_{broad} of the broad Hα profile. Figure 4 shows the corresponding light curves obtained over the complete monitoring campaign.

The mean cadence of the observations during the monitoring campaign was based on the results from Schimoia et al. (2012). In this previous work, we did not observe any significant Hα variations within a time interval of seven days. We therefore planned the monitoring campaign to obtain an optical spectrum with SOAR once every 8 days. As the X-rays usually show shorter variability timescale than the optical in AGNs, we requested a *Swift* observation once every four days whenever possible.

For the high-energy continuum emission, 45 *Swift* observations were obtained in each of two bands, the XRT (0.3–10 keV) and UVOT/M2 band ($\lambda_0 \approx 2246$ Å, FWHM ≈ 510 Å), with a mean time interval of ~4.2 days and minimum and maximum time intervals of ~3 and 8 days, respectively. The Hα light curve comprises 23 observations with a mean time interval between them of ~7.5 days, with minimum and maximum time intervals between two consecutive observations of ~1 and 20 days, respectively.

We characterize the variability of each light curve using the same parameters as O'Brien et al. (1998). The results are given in Table 4, where N is the number of epochs, $\overline{F}$ and σ_F are, respectively the mean flux and standard deviation, and Δ is the mean measurement uncertainty. The parameter F_{var} is an estimate of the amplitude of the variability
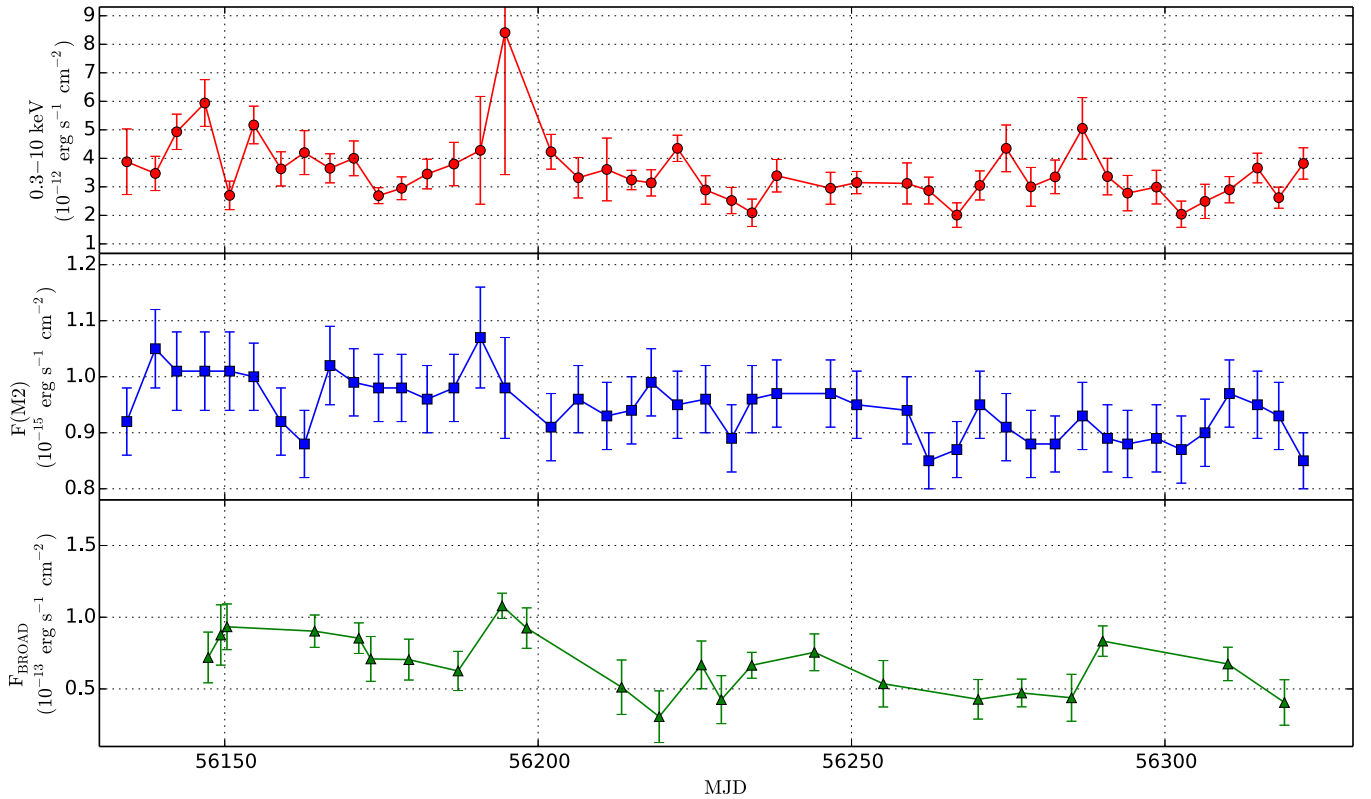
Figure 4. Light curves. Top: integrated flux of the *Swift*/XRT X-ray band, 0.3–10 keV. Middle: UV integrated flux, from the M2 band (∼2246 Å) of *Swift*/UVOT. Bottom: integrated Hα broad-line flux. The largest average variation was observed for the Hα profile, of 20%, followed by the X-rays, which varied by 13%, while the UV did not show significant variation.

Table 4
Variability Parameters

Feature	N	$\overline{F}$	σ_F	Δ	$F_{\rm var}$ (%)	$R_{\rm max}$
XRT[a]	45	3.54	1.1	1.0	13.18	4.18
$F(M2)$[b]	45	9.44	0.52	0.62	INDEF	1.26
$F_{\rm broad}$[b]	23	6.72	2.01	1.43	20.44	3.52

Notes.
[a] $\overline{F}$, σ_F, and Δ are in units of 10^{-12} erg s^{-1} cm^{-2}.
[b] $\overline{F}$, σ_F, and Δ are in units of 10^{-14} erg s^{-1} cm^{-2}.

relative to the mean flux, corrected by the uncertainties in the measurements, i.e.,

$$F_{\rm var} = \frac{\sqrt{\sigma_F^2 - \Delta^2}}{\overline{F}}. \qquad (1)$$

The parameter $R_{\rm max}$ is the ratio between the maximum and minimum fluxes in the light curve.

3.2.1. X-Ray

The X-ray variations (Figure 4) were of very low amplitude, with $F_{\rm var} \approx 13\%$. There were two periods of large changes, a large decrease followed by a large increase in flux around MJD56150 and another increase followed by a rapid decrease around MJD56194. These variations imply that the X-ray emitting structure must be smaller than four light days. We note that there is an ultra-luminous X-ray source (ULX) located approximately 27″ away from the nucleus, as pointed out by Nemmen et al. (2006). As the *Swift* measurements employ an

aperture of 47″ radius, this source is included in our measured X-ray flux. We have used the information provided by Nemmen et al. (2006) to estimate an upper limit of ∼8% to the flux contributed by this ULX to our measurements. If we correct our measurements by this constant contribution, we expect that $F_{\rm var} \approx 15\%$.

3.2.2. UV

The $F_{\rm var}$ parameter for the M2 *Swift* band is undefined because the variations in the UV flux are smaller than the uncertainties of these measurements.

Nemmen et al. (2006) have used an *Hubble Space Telescope* STIS UV/optical spectrum of the nucleus of NGC 1097 as part of the nuclear spectral energy distribution (SED). With data from radio wavelengths to X-rays, they then modeled the nuclear SED as originating in a RIAF plus the contribution from a radio jet, including also the continuum of the part of the disk which emits also the double-peaked line. Besides these components, it is also necessary to include the contribution of a nuclear starburst (Storchi-Bergmann et al. 2005) to reproduce the UV spectral range. The derived contributions of each of these structures to the luminosity at 2246 Å are $L_{\rm RIAF} = 1.26 \times 10^{40}$ erg s^{-1} from the RIAF, $L_{\rm jet} = 2.57 \times 10^{39}$ erg s^{-1} from the radio jet, $L_{\rm disk} = 5.25 \times 10^{34}$ erg s^{-1} from the thin disk, and $L_{\rm star} = 2.04 \times 10^{40}$ erg s^{-1} from the compact nuclear starburst. We thus conclude that, in the observed UV band, the nuclear starburst, which has a projected distance to the nucleus smaller than 9 pc (Storchi-Bergmann et al. 2005), dominates the luminosity. As the light from the starburst does not vary on the timescales we are considering, it can be concluded that any eventual variation
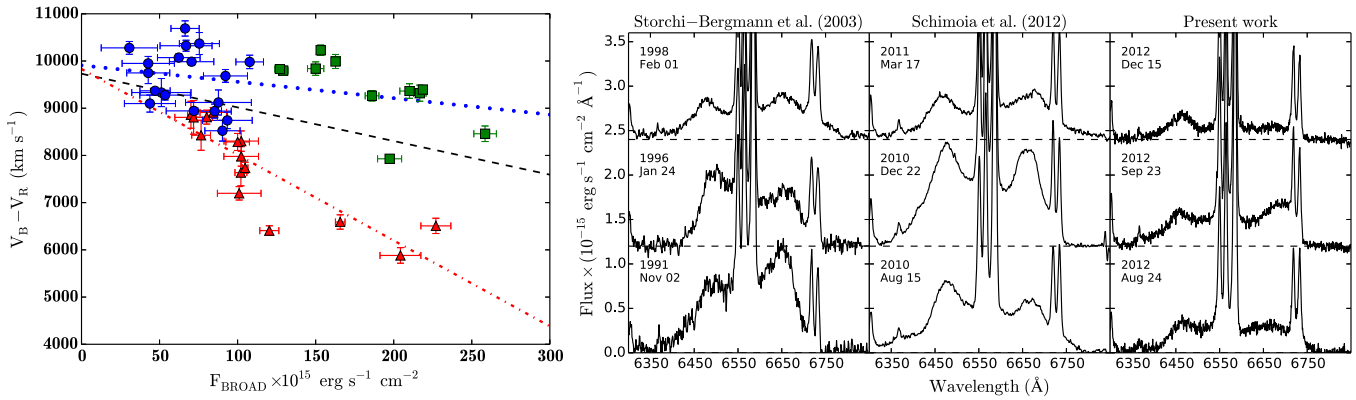
Figure 5. Left: comparison of the relation between the integrated Hα flux, F_{broad}, and velocity separation between the blue and red peaks, $\Delta V = V_B - V_R$, for three different monitoring campaigns. The data from the present work are shown as blue circles; the data from Storchi-Bergmann et al. (2003) are shown as red triangles, and the data from Schimoia et al. (2012) are shown as green squares. The comparison shows that during this campaign F_{broad} remained at the lowest fluxes ever seen while $V_B - V_R$ was at a very large separation. This trend is in agreement with that of the previous observations. The blue dotted line represents the linear regression for the data from Schimoia et al. (2012) + that of this work ($r \sim -0.343$); while the dot–dashed line is the linear regression for the data from Storchi-Bergmann et al. (2003) alone ($r \sim -0.823$). The black dashed line is the linear regression for all the data together ($r \sim -0.354$). Right: three representative profiles of each of the three time periods covered by our previous and present work.

of the AGN in this band is probably heavily diluted by the starburst continuum and cannot be detected.

3.2.3. The Hα Emission Line

As we can see in Figure 2, the Hα profile and flux have varied on the shortest timescales probed by the observations. The broad-component flux F_{broad} varied overall by approximately ~20% ($F_{var} = 20.44\%$) with respect to the mean. The two most remarkable increases in F_{broad} occurred in the interval MJD56187–56194 and MJD56285–56290, when the line flux increased by ~70% in 7 days and by ~90% in 5 days, respectively, as seen in Figures 2 and 4. We conclude that a substantial portion of the broad-line luminosity comes from a region that has a size less than 5 light days.

4. DISCUSSION

The double-peaked Hα profile of NGC 1097 has been monitored by our group for more than 20 yr (Storchi-Bergmann et al. 1993, 1995, 1997, 2003). Recently we reported the discovery of short-timescale variability (Schimoia et al. 2012) of ~7 days, consistent with the shortest timescale variations detected here of ≲5 days. Another previous finding was an inverse correlation between F_{broad} and the velocity separation between the blue and red peaks, $\Delta V = V_B - V_R$. This inverse correlation supports the reverberation scenario: when the ionizing flux is low, the innermost parts of the accretion disk are relatively more important and the profile becomes weaker and broader, when the ionizing flux is high the inner disk becomes more highly ionized, therefore the bulk of the Balmer line emission moves to larger radii (Dumont & Collin-Souffrin 1990) and the profile becomes both stronger and narrower.

Figure 5 shows, in the left panel, a comparison of the measurements of F_{broad} and ΔV of the present and previous works. The right panel shows three typical profiles for each of the three epochs we have collected the data.

The left panel of Figure 5 shows that in the current campaign, the broad Hα flux F_{broad} reached historically low levels and remained low throughout the campaign, with variations comparable to or just barely larger than the uncertainties in the measurements. The separation ΔV between the blue and red peaks

was also at the largest values we have ever observed in this source, what is still consistent with the reverberation scenario.

We now investigate the significance of the inverse correlation between the integrated flux of the Hα double-peaked line and the velocity separation of the blue and red peaks. Figure 5 (left) shows that there is a distinct behavior between the data from Storchi-Bergmann et al. (2003) (red triangles)—taken between 1991 and 2002, and that from our more recent studies, corresponding to the period between 2010–2013, including both the data from Schimoia et al. (2012) and that of the present work (blue circles and green squares).

Between these two data sets there is a temporal gap of approximately 7–8 yr. The right panels of Figure 5 show that in the first data set (1991–2002) the profile showed large variations, both in flux and peak separation, with a strong inverse correlation between the two. In the more recent observations that begun in 2010, the profiles became broader. In order to investigate the significance of the inverse correlation, we have grouped the data as follows: (1) only the data from Storchi-Bergmann et al. (2003); (2) only the most recent data of Schimoia et al. (2012) + that of the present work; and (3) all the data together. The resulting linear regressions are shown as dashed lines in Figure 5.

We have calculated the correlation coefficient and respective significance for the three different groups of data above:

1. For the data from Storchi-Bergmann et al. (2003) alone we found a linear correlation coefficient $r = -0.823^{+0.034}_{-0.038}$, which implies significance levels from 99.95% to 99.99%;
2. For the data from Schimoia et al. (2012) plus that of this work we found a correlation coefficient $r = -0.343^{+0.049}_{-0.050}$, which gives significance levels from 89.25% to 97.17%;
3. For all data together we found a correlation coefficient of $r = -0.354^{+0.029}_{-0.029}$, and the respective significance levels are 97.05% and 99.06%.

Thus we conclude that for any set of data there is an inverse correlation with a significance level ≳90%, while for the complete data set the correlation is ~97%. The data are thus consistent with a low-flux state corresponding to the widest separation between the two peaks, which leads us to the conclusion that the overall data are consistent with the reverberation scenario.

4.1. An Accretion Disk Model

In order to test further the scenario we have proposed for the accretion disk (Schimoia et al. 2012), we modeled the Hα profiles using the accretion disk model described by Gilbert et al. (1999), Storchi-Bergmann et al. (2003), and Schimoia et al. (2012). In this formulation, the broad double-beaked emission line originates in a relativistic Keplerian disk of gas surrounding the SMBH. The line-emitting portion of the disk is circular and located between an inner radius ξ_1 and an outer radius ξ_2 (where ξ is the disk radius in units of the gravitational radius $r_g = GM_{BH}/c^2$, c is the speed of light, G is the gravitational constant, and M_{BH} is the mass of the black hole). The disk has an inclination i relative to the line of sight (i.e., zero degrees is face-on). Superimposed on the axisymmetric emissivity of the circular disk, there is a perturbation in the form of a spiral arm. We adopted the "saturated spiral model" (Schimoia et al. 2012) for the total emissivity of the accretion disk, as it best reproduces the data. This emissivity law is given by

$$\epsilon(\xi, \phi) = \epsilon(\xi) \left\{ 1 + \frac{A}{2} \exp\left[-\frac{4\ln 2}{\delta^2}(\phi - \psi_0)^2 \right] \right.$$
$$\left. + \frac{A}{2} \exp\left[-\frac{4\ln 2}{\delta^2}(2\pi - \phi + \psi_0)^2 \right] \right\}, \quad (2)$$

where

$$\epsilon(\xi) = \begin{cases} \epsilon_0 \xi^{-q_1}, & \xi_1 < \xi < \xi_q \\ \epsilon_0 \xi_q^{-(q_1 - q_2)} \xi^{-q_2}, & \xi_q < \xi < \xi_2 \end{cases} \quad (3)$$

is the axisymmetric emissivity of the disk. The parameter ξ_q is the radius of maximum emissivity, or saturation radius, at which the emissivity law changes; q_1 is the index of the emissivity law for $\xi_1 < \xi < \xi_q$; q_2 is the index for $\xi_q < \xi < \xi_2$. A is the brightness contrast between the spiral arm and the underlying disk, and the expression between square brackets represents the decay of the emissivity of the arm as a function of the azimuthal distance $\phi - \psi_0$ from the ridge line to both sides of the arm, assumed to be a Gaussian function with FWHM = δ (azimuthal width).

The relation between the azimuthal angle ϕ_0 and the angular position ψ_0 of the ridge of emissivity on the spiral arm is given by

$$\psi_0 = \phi_0 + \frac{\ln(\xi/\xi_{sp})}{\tan p}, \quad (4)$$

where ϕ_0 is the azimuthal angle of the spiral pattern, p is the pitch angle, and ξ_{sp} is the innermost radius of the spiral arm.

The specific intensity from each location in the disk, in the frame of the emitting particle is calculated as

$$I(\xi, \phi, \nu_e) = \frac{\epsilon(\xi, \phi)}{4\pi} \frac{e^{-(\nu_e - \nu_0)^2/2\sigma^2}}{(2\pi)^{1/2}\sigma}, \quad (5)$$

where ν_e is the emission frequency and ν_0 is the rest frequency corresponding to Hα λ6564.6 and σ is the local "broadening parameter" (Chen & Halpern 1989).

We fixed the following model parameters: $q_1 = -2.0$, $q_2 = 3.0$, $\xi_{sp} = \xi_1$, $p = 50°$, $\delta = 70°$ and $i = 34°$, which are the same values adopted in previous works (Storchi-Bergmann et al. 2003; Schimoia et al. 2012). Thus, the only parameters we allowed to vary are A, ξ_q and ϕ_0. In practice, ξ_q regulates the width of the profile: when ξ_q is closer to ξ_1 the profile is broader,

Table 5
Parameters of the Accretion Disk Model

| UT Date	MJD	ξ_q	$\phi_0 - 760°$ (°)	A
2012 Aug 7	56147.356	550	15	0.2
2012 Aug 9	56149.368	570	20	0.2
2012 Aug 10	56150.360	580	20	0.2
2012 Aug 24	56164.349	580	30	0.5
2012 Aug 31	56171.388	570	35	0.5
2012 Sep 3	56173.305	550	35	0.8
2012 Sep 8	56179.370	550	40	0.8
2012 Sep 16	56187.222	540	45	2.0
2012 Sep 23	56194.256	580	50	2.5
2012 Sep 27	56198.175	570	50	1.5
2012 Oct 12	56213.316	525	60	1.5
2012 Oct 18	56219.316	500	65	1.5
2012 Oct 25	56226.048	545	70	0.3
2012 Oct 28	56229.229	515	75	0.5
2012 Nov 2	56234.086	545	75	0.2
2012 Nov 12	56244.074	560	80	0.2
2012 Nov 23	56255.068	530	90	0.0
2012 Dec 8	56270.206	515	100	0.0
2012 Dec 15	56277.142	520	105	0.0
2012 Dec 23	56285.097	515	110	0.0
2012 Dec 28	56290.074	570	115	0.0
2013 Jan 17	56310.047	545	130	0.0
2013 Jan 26	56319.067	510	135	0.0

Notes. The date of observations are given in Column 1 while Column 2 gives the Modified Julian Date (JD−2400000.5). The resulting parameters of the modeling are given in the following columns: Column 3 gives the radius of maximum emissivity of the accretion disk, Column 4 gives the azimuthal orientation of the spiral arm, and Column 5 gives the contrast between the spiral arm and the underlying disk.

when ξ_q is closer to ξ_2 the profile becomes narrower; ϕ_0 is the orientation of the spiral pattern and by allowing this parameter to increase monotonically, we can reproduce the variation of the relative intensity of the blue and red peaks as due to the rotation of the spiral arm.

For direct comparison with the scenario proposed by Schimoia et al. (2012), we adopt their derived angular velocity of the spiral arm, of $\dot{\phi}_0 \approx 0°.680$ day^{-1}, which corresponds to a rotation period of ~18 months. Using this prescription, we estimate the value of ϕ_0 for the first optical observation (MJD56147) as 775°, which means that the spiral arm should have completed one rotation since the last observation of Schimoia et al. (2012) for which $\phi_0 = 400°$. The best-fitting models are compared with the observed line profiles in Figure 2, and the corresponding parameter values are listed in Table 5. The disk emissivity for each epoch is illustrated in Figure 6.

As can be seen in Figure 2, the model can indeed reproduce the observed variations of the double-peaked profile. We have tested many values for ξ_q in the range between the inner and outer radius, $\xi_1 = 450$ and $\xi_2 = 1600$. However, we achieved the best fits by keeping ξ_q close to the inner radius, in the range $\xi_q \sim 500$–600. This is consistent with the fact that during the monitoring campaign we observed the broadest profiles ever seen for this object.

In order to improve the fitting we also had to apply an overall blueshift of about -250 km s^{-1} to all model profiles. Such a velocity shift has been noted in our previous studies (Storchi-Bergmann et al. 2003; Schimoia et al. 2012), in which they were attributed to possible winds from the accretion disk. Another
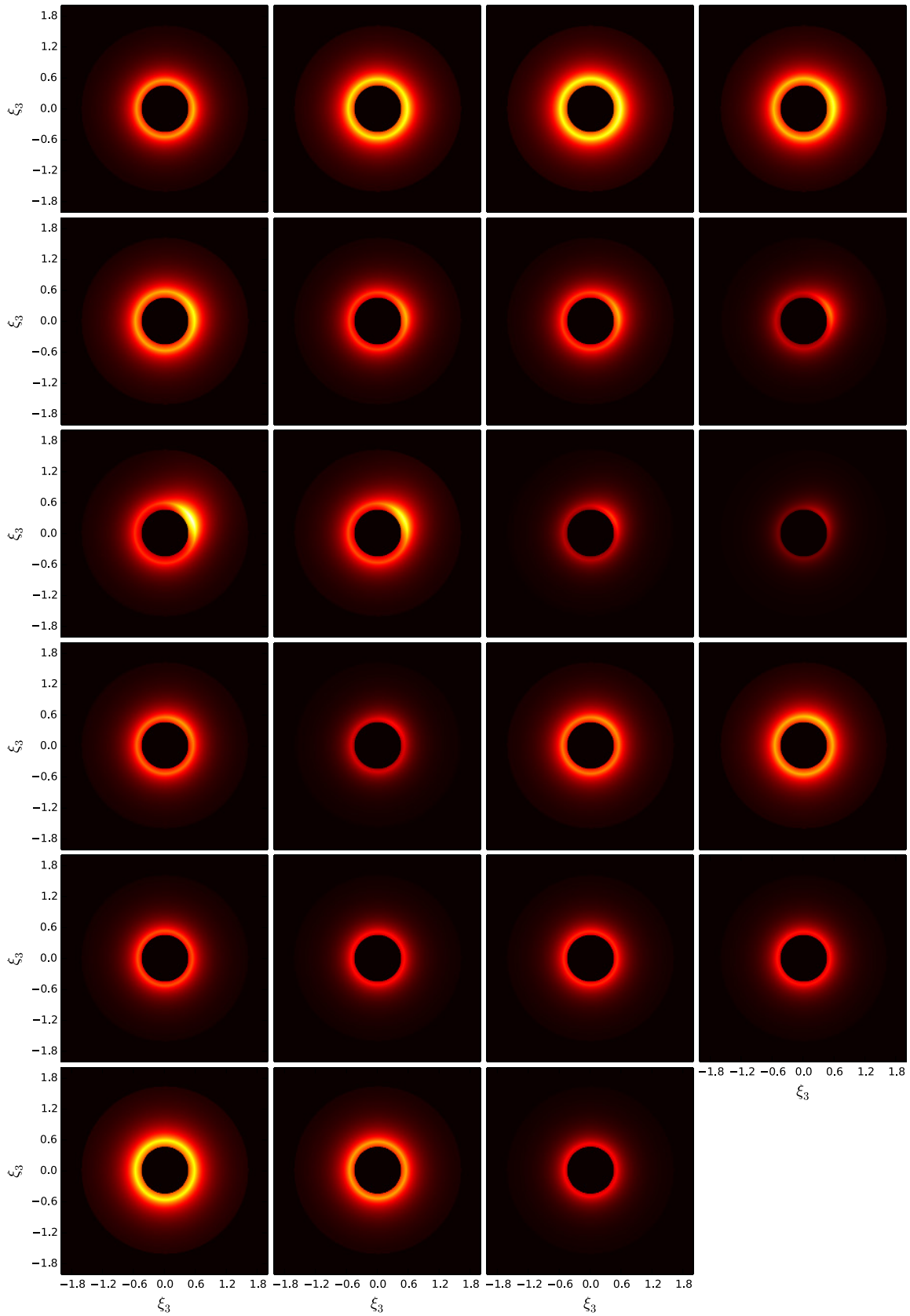
Figure 6. Image showing the disk emissivity utilized to model the double-peaked profile for each epoch of observation of Figure 2. White represents the brightest regions, and the observer is to the bottom. The disk parameters for these epochs are listed in Table 5. On each frame the axis is expressed in terms of $\xi_3 = 10^{-3}\xi$.
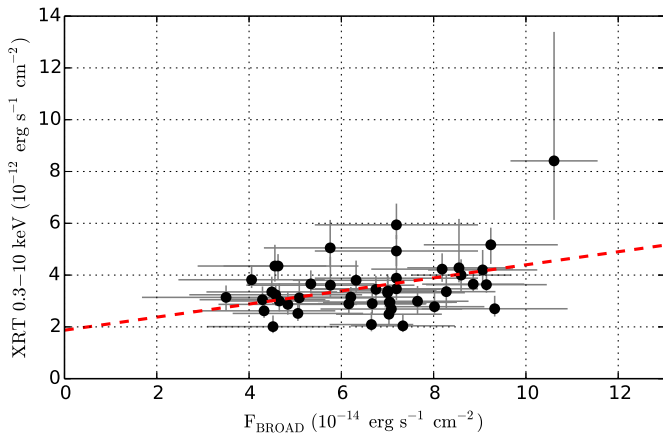
Figure 7. Correlation between X-ray and optical data, where black points represent the fluxes of the X-ray band and the broad profile for the same MJD (after interpolation of the optical light curve to match the epochs of *Swift* observations). The red dashed line is the best linear correlation between the data. The median value of the correlation coefficient is $r = 0.253^{+0.105}_{-0.133}$ which corresponds to a level of significance of 56.8%–98.4%.

possible explanation for the velocity shifts is the presence of the spiral pattern, since the spiral arm also slightly modifies the velocity field and makes it depart from a pure Keplerian velocity field. We note that some epochs require blueshifts somewhat higher or lower than $-250\,\mathrm{km\,s^{-1}}$; however, the corresponding improvements in the fit are smaller than the uncertainties. Thus, we adopt the mean blueshift value of $-250\,\mathrm{km\,s^{-1}}$.

Modeling the present data revealed that the parameter ξ_q—the "break" radius, corresponding to the region with strongest emission in the disk—must be kept close to the inner radius in order to reproduce the observed double-peaked profiles. This result is consistent with the scenario in which the central ionizing source is faint and able to power just the innermost region of the accretion disk. The mean value of ξ_q over all the observations is $\overline{\xi_q} = 545 \pm 25$. Assuming the black hole mass is $M_{\mathrm{BH}} = 1.2 \times 10^8\,M_\odot$ (Lewis & Eracleous 2006), at this radius the dynamical timescale of the accretion disk is $\tau_{\mathrm{dyn}} \approx 3$ months and the rotation period ($2\pi\,\tau_{\mathrm{dyn}}$) is $\sim$18 months, which is consistent with the estimated rotation period for the spiral arm. A property of the double-peaked profile that varies on this timescale is the relative intensity of the blue and red peaks: for instance, from MJD56194 to MJD56277 (see Figure 2) the profile changed from a dominant red peak to a dominant blue peak in $\sim$3 months. We note that the light travel timescale, at $\xi_q = 545$ is just 4 days, which is consistent with the upper limit of $\sim$5 days for the timescale for the Hα flux variations.

4.2. Correlation Between X-Rays and Hα

In order to look for a direct reverberation signal between the X-rays (presumably emitted by the RIAF) and the response of the line-emitting portion of the disk, we applied the interpolated cross-correlation function method (Gaskell & Peterson 1987; White & Peterson 1994; Peterson et al. 1998, 2004) between the X-ray and Hα light curves. Unfortunately, we are unable to constrain the lag between the X-ray and Hα light curves. We are similarly unable to constrain any possible lag between the X-rays and the UV continuum. The main reason that the time-series analysis fails to yield results is primarily the absence of strong flux variations in every band in this campaign. It also seems apparent that, at least in this low-luminosity state, the time sampling was not frequent enough. This conclusion is supported by the fact that we could detect significant variations in the

X-rays and Hα light curves on time intervals as short as our mean sampling time interval.

In order to take into account the effect of the uncertainties of the flux measurements in the correlation, we proceeded as follows. Before calculating the correlation coefficient, we scattered each flux measurement using a Gaussian probability distribution in which the mean value of the Gaussian corresponded to the value of the flux measurement and the root mean square of the Gaussian corresponded to the mean squared value of the lower and upper uncertainties. We repeated this process 10^5 times and calculated the median value for the distribution of values of the correlation coefficient as $\bar{r} = 0.253^{+0.105}_{-0.133}$. We show the correlation between the X-ray and optical data in Figure 7. The upper and lower limits correspond to $\pm 34.1\%$ of the distribution around the median. The lower and upper limits for the correlation coefficient imply a significance level of 56.8%–98.4%.

In order to take into account the effect of the uncertainties of the fluxes measurements in the correlation, we proceeded as follows: before calculating the correlation coefficient, we scattered each flux measurement using a Gaussian probability distribution in which the mean value of the Gaussian corresponded to the value of the flux measurement and the root mean square of the Gaussian corresponded to mean squared value of the lower and upper uncertainties. We repeated this process 10^5 times and calculated the median value for the distribution of values of the correlation coefficient as $\bar{r} = 0.253^{+0.105}_{-0.133}$. The upper and lower limits correspond to $\pm 34.1\%$ of the distribution around the median. The lower and upper limits for the correlation coefficient imply a significance level of 56.8%–98.4%.

We can thus conclude that there is a marginal correlation between the X-ray and Hα flux variations; the variations are not completely random. Nevertheless the correlation is not tight enough to confirm that the two fluxes vary together. The weakness of the correlation is almost certainly attributable to the low amplitude of the variations during the monitoring campaign. The lack of variability in the UV precluded any similar analysis in that band.

4.3. Comparison with other Objects and Accretion Disk Models

Monitoring of "double-peaked" emitters have been used as a probe for testing accretion disk models and to understand what are the physical mechanisms responsible for the observed changes in the double-peaked profiles. In this subsection we make a comparison between the observed properties of the NGC 1097 double-peaked profile and two other also very well studied double-peaked emitters: Arp 102B and 3C390.3.

In the case of 3C 390.3, many works have reported spectroscopic long-term monitoring (years do decades) (Shapovalova et al. 2001; Sergeev et al. 2002; Shapovalova et al. 2010) or short-term monitoring (a few months) (Dietrich et al. 2012) of the AGN optical continuum around 5100 Å and the variations of the broad Balmer double-peaked emission lines, Hα and Hβ. Common to these works is the conclusion that the broad double-peaked Balmer lines flux variations do follow the optical continuum variations with time delays of $\tau(\mathrm{H}\alpha) \gtrsim 56$ days and $\tau(\mathrm{H}\beta) \gtrsim 44$ days. Also, Dietrich et al. (1998) found that the flux variations of the Balmer lines of Arp 102B seems to be correlated with the X-ray flux variations with a time delay of $\sim$20 days. However, for the case Arp 102B the variations of the flux of the Balmer broad double-peaked emission lines do not appear to be strongly correlated with the variations of the AGN optical continuum (Shapovalova et al. 2013). In spite

of the weak correlation, the authors estimate a time delay of $\tau(H\beta) \sim 20$ days.

In the case of NGC 1097, we were never able to detect the AGN optical continuum (Storchi-Bergmann et al. 1993, 2003; Schimoia et al. 2012), and this was the motivation for us to look for the continuum in X-rays and UV. Unfortunately, the variations were small during our campaign, but in Section 4.2 we have nevertheless shown that the profile variations are weakly correlated with the X-ray continuum variations, indicating that the X-rays could indeed be the driver of the double-peaked profile.

In the case of Arp 102B the variations of the relative intensity of the blue and red peaks were first modeled by Newman et al. (1997) in the context of a relativistic accretion disk in which the non axisymmetric emissivity part of the disk has the shape of a *hot spot* that rotates in the disk around the central SMBH in the dynamical timescale. In the case of 3C390.3 the *hot spot* model have been used to explain the observed flux "outbursts" of the blue peak of the profile (Jovanović et al. 2010). Lewis et al. (2010) have reported a long-term monitoring of a few radio galaxies in which the double-peaked profiles display small flux *bumps* that move in the velocity space and are attributed to hot spots in the accretion disk. Nevertheless, in almost all cases the hot spots are short lived: they have been observed to appear and are more likely to last from several months to a few years. In contrast, the alternating relative intensity of the blue and red peaks of NGC 1097 have lasted for more than 20 yr, suggesting that the features producing the variation of the relative intensity of the blue and red peaks are longer lived than the hot spots observed in other double-peaked emitters. The variations in the relative intensity of the blue and red peaks in NGC 1097 have been clearly observed both when the flux of the broad line is in a high state (higher line flux and narrower profile) as well as when the flux is in a low state (low line flux and broader profile). On the other hand, we note that the emissivity of the *saturated spiral model* adopted in our modeling is not that different from that of a *hot spot*, in the sense that the spiral arm + broken power-law emissivity component can effectively concentrate the non-axisymmetric emissivity in a structure very similar to a hot spot (see Figure 6, MJD56194). Nevertheless, we favor the scenario of the *saturated spiral model* for NGC 1097 due the fact that the fast timescale variations of the profile, namely in the velocity separation of the peaks and integrated flux of the broad profile, occur in timescales of a few days to a few weeks. At these short timescales, these variation can only be attributed to changes in the illumination/ionization of the disk, which have been modeled by changing the break radius, ξ_q, while the rotation of the non axissymetric pattern allow us to simultaneously model the variations of the relative intensity of the blue and red peaks.

Finally, we point out that at some epochs there is a flux excess in the high velocities of the blue wing of the double-peaked profile (see Figure 2, for instance MJD56194 and 56290), that was also observed in previous works (Storchi-Bergmann et al. 2003; Schimoia et al. 2012). The origin of this excess is not completely understood. In Storchi-Bergmann et al. (2003) it was proposed that it could be due to the presence of a wind emanating from the disk, what is not taken into account in the model.

5. CONCLUSIONS

We monitored the AGN in NGC 1097 for ~6 months, from 2012 August to 2013 February, in three spectral bands: in the

X-ray (0.3–10 keV), using the *Swift*/XRT, in the UV, using the *Swift*/UVOT telescope, and in the double-peaked Hα profile, with data from the SOAR and Gemini-South telescopes. Our main conclusions are:

1. The X-ray fluxes varied on the shortest timescale probed by the observations, 4 days, indicating that the emitting structure has a size smaller than 4 light days; the maximum variation observed between two consecutive dates was 97%, but the average variation over the whole period was only 13%.

2. The Hα flux also varied on the shortest timescale probed by the observations, ~5 days. The maximum variation observed was 90%, but the average variation over the whole period was 20%.

3. To within the uncertainties, the UV flux did not vary. This can be due to the contribution of the compact nuclear starburst previously found within the inner 9 pc, that dominates the UV continuum emission, and is probably diluting the contribution of a variable source.

4. Although we have not found a clear reverberation signal in our most recent data, when we consider this data together with the previous ones from epochs 1991–2001 and 2010–2012, they are consistent with the reverberation scenario, as we can still observe, in the overall data, an inverse correlation between the Hα flux and the separation between the red and blue peaks of the Hα profile, as noted in previous studies.

5. We were able to reproduce the variations of the double-peaked profile using the same accretion disk model of Schimoia et al. (2012); in particular, we kept the same inner and outer radii, as well as the 18 month rotation period for a spiral arm in the disk, that, combined with variations in the contrast of the spiral arm, successfully reproduces the variation of the relative intensity of the blue and red peaks.

6. The small range of variation of the width of the double-peaked profiles was reproduced by keeping the ξ_q values (radius of maximum emissivity) close to the inner radius. This radius corresponds to a rotation period of 18 months and a light travel time of ~4 days, in agreement with the shortest variation timescales observed.

7. We find only a marginal correlation between the X-ray and Hα flux variations, although the analysis reveals the need for more frequent monitoring of this source, particularly when it is in such a low-luminosity state.

The presence of some correlation between the X-ray flux and the broad Hα profile, even though we could get only an upper limit on the shortest variation timescale, leads us to the conclusion that the variations of the broad Hα line profile do follow the variations of the X-ray flux. But we also note that the Hα flux remained at the lowest levels we have ever observed, and the blue and red peaks of the double-peaked profile remaining at the widest separation. This indicates that we have caught the AGN in NGC 1097 in a very low activity state, in which the ionizing source was very weak and capable of ionizing just the innermost part of the gas in the disk. Nonetheless, the data presented here still support the picture in which the gas that emits the double-peaked Balmer lines is illuminated/ionized by a source of high-energy photons which is located interior to the inner radius of the line-emitting part of the disk.

REFERENCES

Breeveld, A. A., Curran, P. A., Hoversten, E. A., et al. 2010, MNRAS, 406, 1687
Burrows, D. N., Hill, J. E., Nousek, J. A., et al. 2005, SSRv, 120, 165
Cardelli, J. A., Clayton, G. C., & Mathis, J. S. 1989, ApJ, 345, 245
Cid, Fernandes, R., Mateus, A., Sodré, L., Stasińska, G., & Gomes, J. M. 2005, MNRAS, 358, 363
Chen, K., & Halpern, J. P. 1989, ApJ, 344, 115
Chen, K., Halpern, J. P., & Filippenko, A. V. 1989, ApJ, 339, 742
Dietrich, M., Peterson, B. M., Albrecht, P., et al. 1998, ApJS, 115, 185
Dietrich, M., Peterson, B. M., Grier, C. J., et al. 2012, ApJ, 757, 53
Dumont, A. M., & Collin-Souffrin, S. 1990, A&A, 229, 313
Eracleous, M., & Halpern, J. P. 1994, ApJS, 90, 1
Eracleous, M., & Halpern, J. P. 2003, ApJ, 599, 886
Frank, J., King, A., & Raine, D. J. 2002, in Accretion Power in Astrophysics (3rd ed.; Cambridge: Cambridge Univ. Press), 398
Gaskell, C. M., & Peterson, B. M. 1987, ApJS, 65, 1
Gezari, S., Halpern, J. P., & Eracleous, M. 2007, ApJS, 169, 167
Gilbert, A. M., Eracleous, M., Filippenko, A. V., & Halpern, J. P. 1999, in ASP Conf. Ser. 175, Structure and Kinematics of Quasar Broad Line Regions, ed. C. M. Gaskell, W. N. Brandt, M. Dietrich, D. Dultzin-Hacyan, & M. Eracleous (San Francisco, CA: ASP), 189
Hill, J. E., Burrows, D. N., Nousek, J. A., et al. 2004, Proc. SPIE, 5165, 217
Jovanović, P., Popović, L. Č., Stalevski, M., & Shapovalova, A. I. 2010, ApJ, 718, 168
Kalberla, P. M. W., Burton, W. B., Hartmann, D., et al. 2005, A&A, 440, 775
Lewis, K. T., & Eracleous, M. 2006, ApJ, 642, 711
Lewis, K. T., Eracleous, M., & Storchi-Bergmann, T. 2010, ApJS, 187, 416
Luo, B., Brandt, W. N., Eracleous, M., et al. 2013, MNRAS, 429, 1479
Narayan, R., & McClintock, J. E. 2008, NewAR, 51, 733
Nemmen, R. S., Storchi-Bergmann, T., Yuan, F., et al. 2006, ApJ, 643, 652
Newman, J. A., Eracleous, M., Filippenko, A. V., & Halpern, J. P. 1997, ApJ, 485, 570
O'Brien, P. T., Dietrich, M., Leighly, K. M., et al. 1998, ApJ, 509, 163
Peterson, B. M., Denney, K. D., De, Rosa, G., et al. 2013, ApJ, 779, 109
Peterson, B. M., Ferrarese, K., Gilbert, K. M., et al. 2004, ApJ, 613, 682
Peterson, B. M., Wandes, I., Horne, K., et al. 1998, PASP, 110, 660
Poole, T. S., Breeveld, A. A., Page, M. J., et al. 2008, MNRAS, 383, 627
Roming, P. W. A., Kennedy, T. E., Mason, K. O., et al. 2005, SSRv, 120, 95
Roming, P. W. A., Koch, T. S., Oates, S. R., et al. 2009, ApJ, 690, 163
Schimoia, J. S., Storchi-Bergmann, T., Nemmen, R. S., Winge, C., & Eracleous, M. 2012, ApJ, 748, 145
Sergeev, S. G., Pronik, V. I., Peterson, B. M., Sergeeva, E. A., & Zheng, W. 2002, ApJ, 576, 660
Shapovalova, A. I., Burenkov, A. N., Carrasco, L., et al. 2001, A&A, 376, 775
Shapovalova, A. I., Popović, L. Č., Burenkov, A. N., et al. 2010, A&A, 517, A42
Shapovalova, A. I., Popović, L. Č., Burenkov, A. N., et al. 2013, A&A, 559, A10
Storchi-Bergmann, T., Baldwin, J. A., & Wilson, A. S. 1993, ApJL, 410, L11
Storchi-Bergmann, T., Eracleous, M., Livio, M., et al. 1995, ApJ, 443, 617
Storchi-Bergmann, T., Eracleous, M., Ruiz, M. T., et al. 1997, ApJ, 489, 87
Storchi-Bergmann, T., Nemmen da, Silva, R., Eracleous, M., et al. 2003, ApJ, 598, 956
Storchi-Bergmann, T., Nemmen, R. S., Spinelli, P. F., et al. 2005, ApJL, 624, L13
Strateva, I. V., Brandt, W. N., Eracleous, M., & Garmire, G. 2008, ApJ, 687, 869
Strateva, I. V., Brandt, W. N., Eracleous, M., Schneider, D. P., & Chartas, G. 2006, ApJ, 651, 749
Strateva, I. V., Strauss, M. A., Hao, L., et al. 2003, AJ, 126, 1720
White, R. J., & Peterson, B. M. 1994, PASP, 106, 879